Proceedings of the
Annual Stability Conference
Structural Stability Research Council
Nashville, Tennessee, March 24-27, 2015

Practical Design of Hollow Structural Shapes by Means of the Overall Interaction Concept

Joanna Nseir[1], Marielle Hayeck[2], Elsy Saloumi[3], Nicolas Boissonnade[4]

Abstract

The present paper is dedicated to the practical design of steel hollow sections. It presents a new design philosophy allowing for a direct prediction of the cross-sectional resistance, whatever the loading, yield stress, manufacturing process, cross-section shape and slenderness.
In particular, the proposed approach is shown to be able to deal with plastic, compact or slender sections through the same simple and straightforward format. As a consequence, the use of the Effective Width Method for slender sections – which are expected to be met more often in practice with the increasing use of high strength steels is no more needed.
In a first step, the paper summarizes the results of an extensive experimental series that helped validating shell FE models. Then, the results of more than 40 000 GMNIA numerical simulations are presented, aiming at characterizing the onset of local buckling with respect to many parameters, such as cross-section shape (square and rectangular tubes), hot-rolled and cold-formed fabrication processes, different types of loading situations (from simple load cases to combined ones), different steel grades and various cross-section dimensions and thicknesses so as to cover "plastic" to "slender" responses of the sections.
These results are later used to assess the merits of the proposed design approach, and excellent performance is demonstrated, both in terms of accuracy and consistency, which is remarkable given the formal simplicity format of the proposed approach.

1. Scope and motivation

The present paper is related to the stability, resistance and design of steel hollow section members. More precisely, the behaviour of hollow sections is investigated through a large experimental campaign aiming at improving the way the performance and the carrying capacity of tubular members are actually characterized, through the development of an original "Overall Interaction Concept" (O.I.C.) (Figure 1). Based on the resistance and stability interaction, the O.I.C. further incorporates the effects of imperfections (non-homogenous material, residual stresses, out-of-straightness…) through the derivation of adequate "interaction curves" used to accurately predict the real behaviour of structural elements. The proposed concept is powerful

[1] Graduate Student, University of Applied Sciences of Western Switzerland, <joanna.nseir@gmail.com>
[2] Graduate Student, University of Applied Sciences of Western Switzerland, <elsysaloumi@gmail.com>
[3] Graduate Student, University of Applied Sciences of Western Switzerland, <marielle_hayeck@hotmail.com>
[4] Professor, University of Applied Sciences of Western Switzerland, <nicolas.boissonnade@hefr.ch>

enough to i) increase accuracy and simplicity through a sound and effective basis, ii) deal with the effects of non-linear material behaviour and local/global coupled instabilities, and iii) advance consistency with the possibility of straightforwardly deal with any load case, including combined ones.

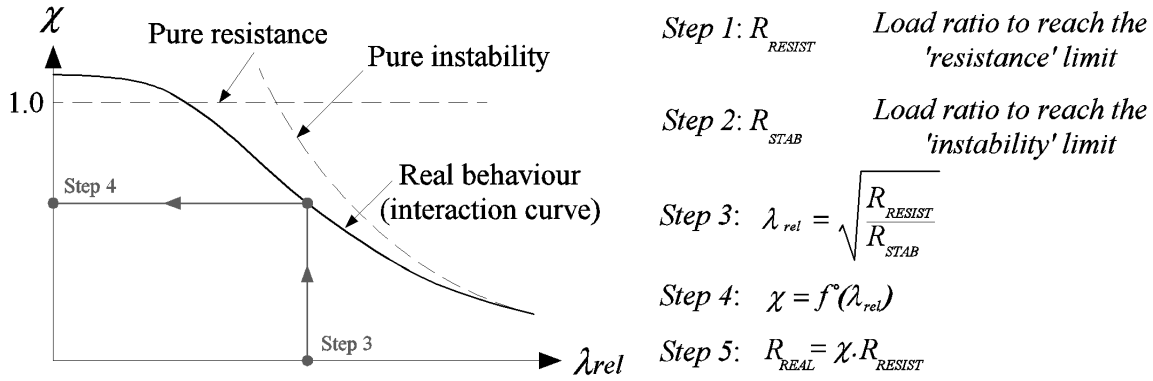

Figure 1: Application steps of the O.I.C.

The O.I.C. suggests to enlarge the field of application of the well-known slenderness-related approach through the use of a generalized relative slenderness λ_{rel}, in which R_{RESIST} represents the factor by which the actual loading has to be multiplied to reach the *resistance* limit (i.e. no instability), while R_{STAB} is the factor characterizing the elastic buckling load. (*instability* limit, i.e. allowable stress is infinite).

The research investigations reported in this paper are relative to a comprehensive test series that aim at providing an experimental reference and assessment to the proposed approach. This experimental campaign comprised 57 cross-sectional tests, as well as preliminary measurements of material properties, residual stresses and geometrical imperfections (section 2); section 3 then presents a comparison between the test results and the predictions of purposely-derived FE models. A consecutive parametric study performed on hot-rolled and cold-formed hollow sections is presented in section 4 so as to investigate the adequacy of the Overall Interaction Concept. Finally, section 5 details the background of the proposed design approach relative to the particular application of the Overall Interaction Concept to cross-sectional resistance.

2. Experimental investigations

2.1 Test program and experimental setup

An experimental program was carried out on a wide variety of tubular cross-sectional shapes (RHS, SHS, CHS)[5] with different fabrication processes and various dimensions (thus local plate slenderness) in order to investigate the influence of local buckling on the plastic, elastic-plastic or slender cross-section response of hollow sections. The main aim of this test campaign was to provide an experimental reference to assess numerical FE models. The testing program comprised 57 tests involving twelve hot-rolled, hot-finished or cold-formed square, rectangular and circular sections (see Table 1).

[5] RHS : Rectangular Hollow Section, SHS : Square Hollow Section, CHS : Circular Hollow Section

Table 1: Test program for cross-sectional tests

Test #	Specimen	Fabrication process	Length [mm]	Load case
1	RHS_LC1_S355CF_200x100x4	Cold-formed	700	N
2	RHS_LC1_S355CF_220x120x6	Cold-formed	700	N
3	RHS_LC1_S355HF_250x150x5	Hot- finished	700	N
4	RHS_LC1_S355HF_200x100x5	Hot- finished	700	N
5	SHS_LC1_S355CF_200x200x5	Cold-formed	700	N
6	SHS_LC1_S355CF_200x200x6	Cold-formed	700	N
7	SHS_LC1_S355HF_200x200x5	Hot- finished	700	N
8	SHS_LC1_S355HF_200x200x6.3	Hot- finished	700	N
9	CHS_LC1_S355CF_159x6.3	Cold-formed	700	N
10	CHS_LC1_S355HF_159x6.3	Hot-Rolled	700	N
11	CHS_LC1_S355HF_159x5	Hot-Rolled	700	N
12	CHS_LC1_S355HF_159x7.1	Hot-Rolled	700	N
13	RHS_LC2_S355CF_200x100x4	Cold-formed	700	$N + M_y$
14	RHS_LC2_S355CF_220x120x6	Cold-formed	700	$N + M_y$
15	RHS_LC2_S355HF_250x150x5	Hot- finished	700	$N + M_y$
16	RHS_LC2_S355HF_200x100x5	Hot- finished	700	$N + M_y$
17	SHS_LC2_S355CF_200x200x5	Cold-formed	700	$N + M_y$
18	SHS_LC2_S355CF_200x200x6	Cold-formed	700	$N + M_y$
19	SHS_LC2_S355HF_200x200x5	Hot- finished	700	$N + M_y$
20	SHS_LC2_S355HF_200x200x6.3	Hot- finished	700	$N + M_y$
21	CHS_LC2_S355CF_159x6.3	Cold-formed	700	$N + M_y$
22	CHS_LC2_S355HF_159x6.3	Hot-Rolled	700	$N + M_y$
23	CHS_LC2_S355HF_159x5	Hot-Rolled	700	$N + M_y$
24	CHS_LC2_S355HF_159x7.1	Hot-Rolled	700	$N + M_y$
25	RHS_LC3_S355CF_200x100x4	Cold-formed	700	$N+ M_y + M_z$
26	RHS_LC3_S355CF_220x120x6	Cold-formed	700	$N + M_y + M_z$
27	RHS_LC3_S355HF_250x150x5	Hot- finished	700	$N + M_y + M_z$
28	RHS_LC3_S355HF_200x100x5	Hot- finished	700	$N + M_y + M_z$
29	SHS_LC3_S355CF_200x200x5	Cold-formed	700	$N + M_y + M_z$
30	SHS_LC3_S355CF_200x200x6	Cold-formed	700	$N + M_y + M_z$
31	SHS_LC3_S355HF_200x200x5	Hot- finished	700	$N + M_y + M_z$
32	SHS_LC3_S355HF_200x200x6.3	Hot- finished	700	$N + M_y + M_z$
33	CHS_LC3_S355CF_159x6.3	Cold-formed	700	$N + M_y + M_z$
34	CHS_LC3_S355HF_159x6.3	Hot-Rolled	700	$N + M_y + M_z$
35	CHS_LC3_S355HF_159x5	Hot-Rolled	700	$N + M_y + M_z$
36	CHS_LC3_S355HF_159x7.1	Hot-Rolled	700	$N + My + M_z$
37	2_SHS_LC1_S355CF_200x200x6*	Cold-formed	700	N

38	2_SHS_LC2_S355CF_200x200x6*	Cold-formed	700	N + M_y
39	2_SHS_LC3_S355CF_200x200x6*	Cold-formed	700	N + M_y +M_z
40	RHS_LC4_S355CF_220x120x6	Cold-formed	700	N + M_y +M_z
41	RHS_LC5_S355CF_220x120x6	Cold-formed	700	N + M_y +M_z
42	RHS_LC6_S355CF_220x120x6	Cold-formed	700	N + M_y +M_z
43	RHS_LC4_S355CF_200x100x4	Cold-formed	700	N + M_y +M_z
44	RHS_LC5_S355CF_200x100x4	Cold-formed	700	N + M_y +M_z
45	RHS_LC6_S355CF_200x100x4	Cold-formed	700	N + M_y +M_z
46	RHS_Stub_S355CF_200x100x4	Cold-formed	600	Stub column
47	RHS_Stub_S355CF_220x120x6	Cold-formed	680	Stub column
48	RHS_Stub_S355HF_250x150x5	Hot- finished	750	Stub column
49	RHS_Stub_S355HF_200x100x5	Hot- finished	600	Stub column
50	SHS_Stub_S355CF_200x200x5	Cold-formed	600	Stub column
51	SHS_Stub_S355CF_200x200x6	Cold-formed	600	Stub column
52	SHS_Stub_S355HF_200x200x5	Hot- finished	600	Stub column
53	SHS_Stub_S355HF_200x200x6.3	Hot- finished	600	Stub column
54	CHS_Stub_S355CF_159x6.3	Cold-formed	480	Stub column
55	CHS_Stub_S355HF_159x6.3	Hot-rolled	480	Stub column
56	CHS_Stub_S355HF_159x5	Hot-rolled	480	Stub column
57	CHS_Stub_S355HF_159x7.1	Hot-rolled	480	Stub column

* The rectangular cross-section 200x200x6 has two test specimens for the first three load cases

Preliminary measurements of geometrical imperfections were achieved, and tensile tests were carried out to determine the material stress-strain behaviour. Stub column tests were also performed for all different cross-section types. As for the main cross-sectional tests, six different load cases (LCs) were distinguished; mono-axial or bi-axial bending with axial compression load cases were considered through the application of eccentrically-applied compression forces. Different M / N ratios have been adopted, in order to vary the distribution of stresses on the flanges and webs, and the following load cases have finally been considered:

- LC1: pure compression N;
- LC2: major-axis bending M_y (50%) + axial compression N (50%)[6];
- LC3: bi-axial bending M_y (33%) + M_z (33%) + axial compression N (33%);
- LC4: minor-axis bending M_z (50%) + axial compression N (50%);
- LC5: bi-axial bending M_y (25%) + M_z (25%) + axial compression N (50%);
- LC6: bi-axial bending M_y (10%) + M_z (10%) + axial compression N (80%).

The mono-axial and the bi-axial-bending with axial compression load cases were obtained through applying compression eccentrically. This procedure of load application seemed to be the

[6] The percentage between brackets indicates the relative level of axial force N_{Ed} / N_{pl} in case of a compression and $M_{Ed,y} / M_{y,el}$ or $M_{Ed,z} / M_{z,el}$ in case of major and minor axis bending respectively.

simplest and most practical way to obtain both axial compression and constant bending moment along the length of the specimens. As shown in Figure 2, the loading rig consisted of a hydraulic jack at the bottom, designed for applying the compressive force, and a top plateau fixed at a prescribed height. Two spherical supports were specially designed to provide pin-pin end restraints for the specimens. End-plates were welded to the profiles with different eccentricities, according to the desired load case. A base plateau was fixed to the hinges with two rails meant for bolting the specimen endplates at the expected location.

The response of each specimen has been carefully monitored and recorded, in view of a comparison with FE models. The end plates and the base plateau had respectively a thickness of 20 *mm* and 60 *mm* and the loading was applied evenly on the ends of the specimen (constant bending moment). Measurements were made for axial shortening / elongation and end plates rotations at both extremities. All cross-section tests have been carried out in a testing machine of 3000 *kN* capacity.

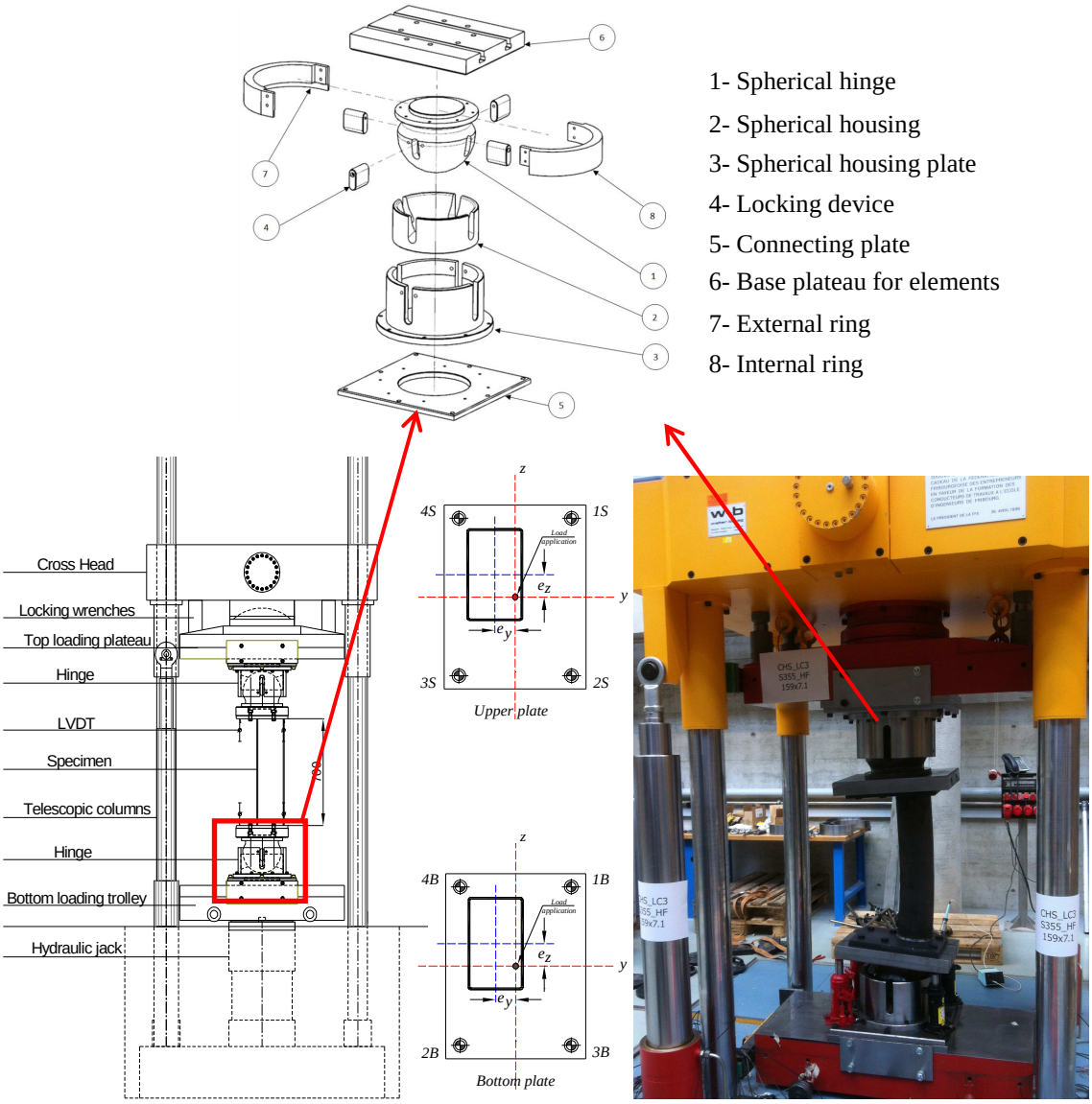

Figure 2: Test setup

2.2 Preliminary measurements

The stress-strain behavior of the tested specimens was captured through 55 tensile tests. For each of the eight square hollow sections (SHS) and rectangular hollow sections (RHS) parent elements, four necked coupons were cut and manufactured from each flat face. In addition, two straight corner coupons were manufactured and tested for each of these sections in order to investigate the increase in strength in the cold-formed corners and to confirm uniform properties in the hot finished corners. Stresses were evaluated through the actual cross-section of each coupon measured before testing. However, for the corner coupons, the area was also determined by combining weight, initial length and density. Typical stress-strain curves measured from hot-finished and cold-formed material are shown in Figure 3a.

The highest stress level reached in corner coupons of cold-formed sections was 15% to 20% higher than the corresponding flat coupons' highest stress level. Such results caused by high cold-work in the corner regions were accompanied by a loss in ductility in a way that none of the corner coupons exceeded strains higher than 5%.

The strip-cutting method has been used to measure both flexural stresses and membrane residual stresses. It consists in a destructive technique relying on the measurement of strains triggered by the release of residual stresses after the cutting of small strips within the cross-section; material relaxation generates either elongation or shortening of the strips due to membrane stresses and a curvature due to flexural stresses. Figure 3b displays an example of the measured residual stresses patterns for a hot-finished square section (membrane residual stresses).

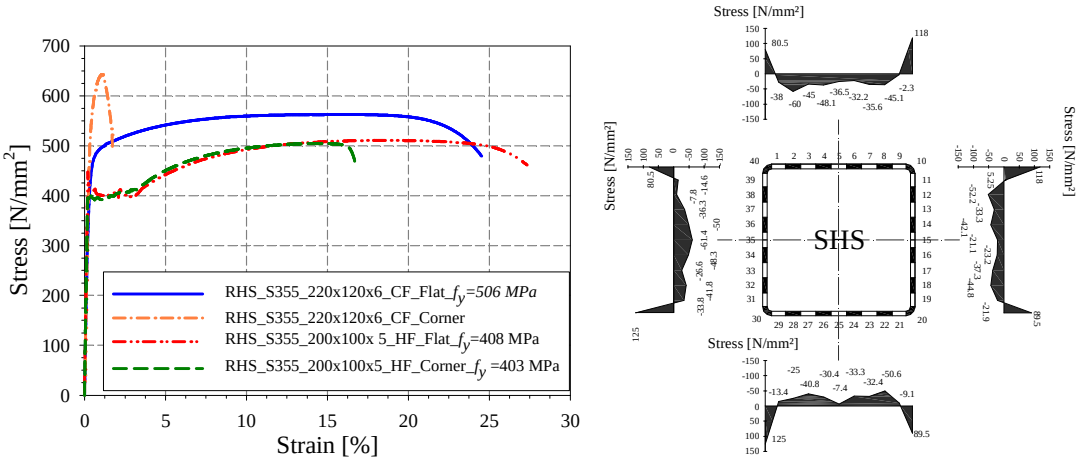

Figure 3: a) Stress-strain curves from flat and corner regions of a cold formed and a hot-formed sections – b) Membrane residual stress measurements, SHS200x200x6.3, Hot-finished

Measurement of geometrical imperfections was achieved by means of an aluminium perforated bar containing 9 equally-spaced variable displacement transducers (LVDTs), the bar being displaced sideways on each specimen's plate (see Figure 5) in order to get 3D geometrical plate representations ((Semi-Comp 2007), (Kettler 2008)); after having measured all faces of a specimen, all information have been gathered in a recomposed specimen that contains the measured local geometrical imperfections. The objective was to provide accurate data for the FE models in a later stage of the investigations. The aluminium bar supporting the LVDTs was

designed so as to be able to move the LVDTs themselves within the bar, and to let the possibility to adjust the position according to the desired height corresponding to the end plate dimensions. An example of a general imperfect shape of the specimen SHS_LC2_200x200x6_CF is shown in Figure 4 with the contour plots of its imperfect plates separately.

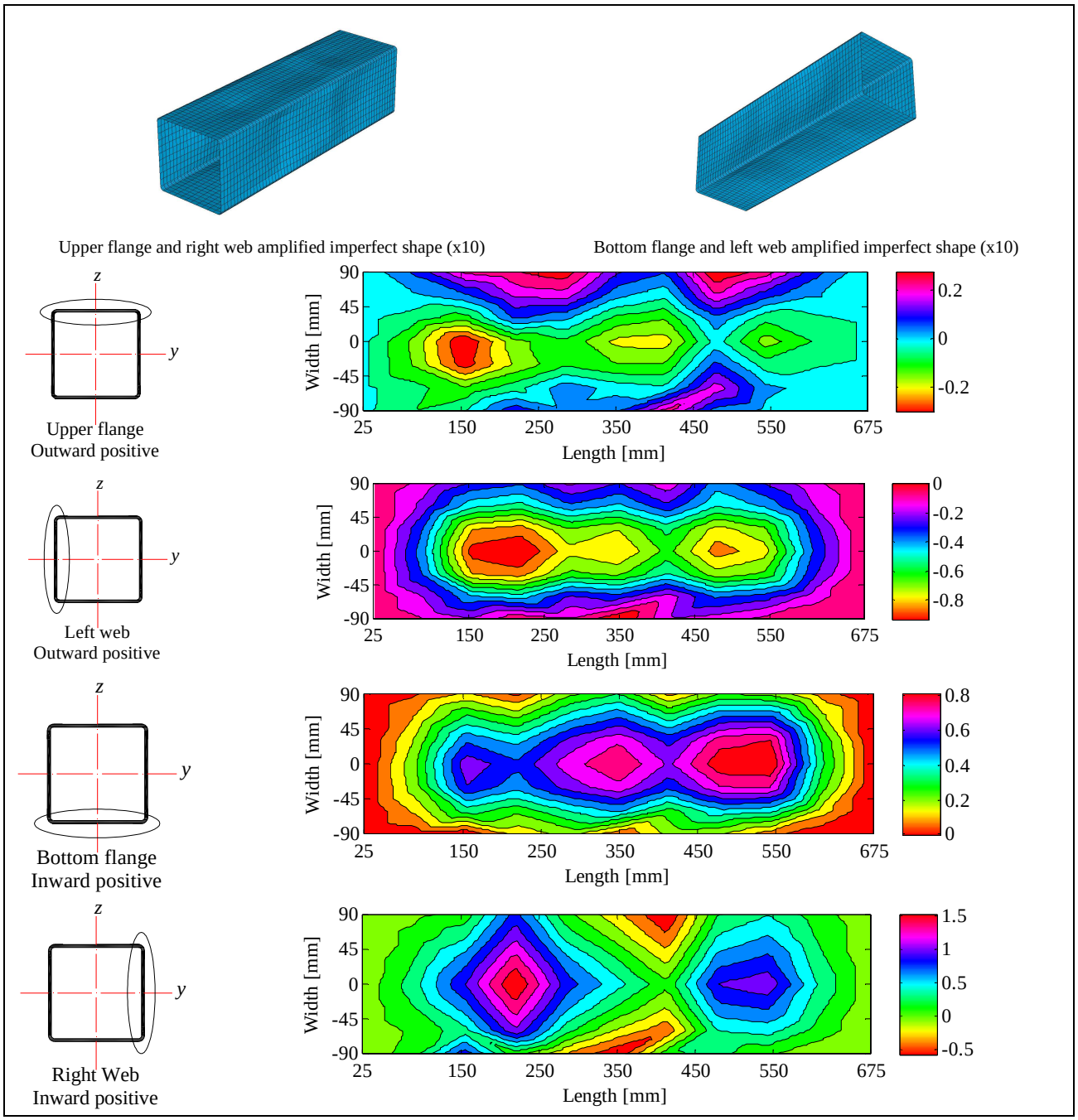

Figure 4: Measured local flange and web geometrical imperfections of specimen SHS_LC2_200x200x6_CF

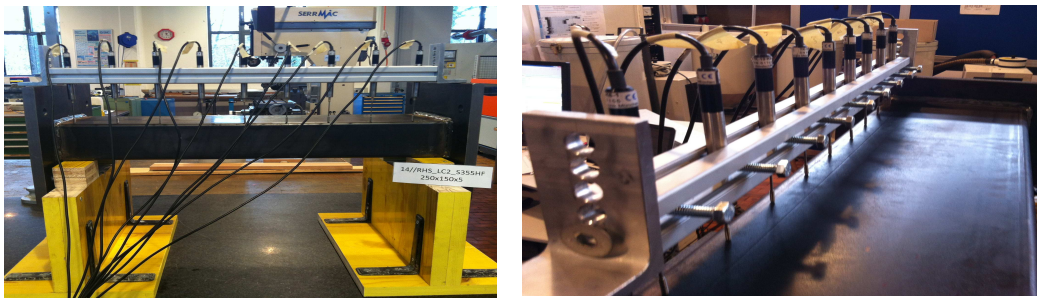

Figure 5: Geometrical imperfections measurement – LVDTs detail bar

12 stub column tests were also performed for each cross-section type in order to determine the average stress-strain relationship over the complete cross-section. The length of each stub column was chosen so as to be about three times the height of the cross section, to avoid global buckling. Two strain gauges have been glued at mid-height of all the elements after polishing and cleaning the surface not only to ensure that compression was being applied concentrically but also to check the load displacement behaviour of the specimen in the elastic range, so as the corresponding Young's modulus to be determined. Four LVDTs were used in order to record the average end-shortening behavior.

Typical failure for stocky sections occurred with a whole cross-section yielded with local buckling at the ends of the specimens ("elephant-foot failure"), whilst for slender sections, local buckling was located at the middle of the specimen. Examples of failure modes are shown in Figure 6.

Figure 6: Failure shapes of the stub columns

2.3 Test results

Four upper LVDTs and four bottom LVDTs were set to record respectively the upper plate rotations and displacements and the bottom plate rotations and displacements. The values recorded with the LVDTs had to be corrected, with respect to the level of rotation reached. All tests were performed in the Structural Engineering Laboratory of the University of Applied Sciences - Fribourg.

LC1

LC2

LC3

Figure 7: Failure modes relative to load cases (LC) 1 2 and 3

The response of each test has been carefully monitored and recorded, in view of the validation of finite element models. The failure modes relative to load cases 1, 2 and 3 are shown in Figure 7. The measured peak loads of all tested specimens are listed in Table 2. Two examples of load-displacement curves are also shown in Figure 8.

Table 2: Comparison of numerical and experimental ultimate loads

Test #	Specimen	Load case	e_z_e_y* [mm]-[mm]	F_{exp} [kN]	F_{FEM} [kN]	F_{exp}/ F_{FEM} [-]
1	RHS_LC1_S355CF_200x100x4	N (100%)	0_0	773	796	0.97
2	RHS_LC1_S355CF_220x120x6	N (100%)	0_0	1594	1651	0.96
3	RHS_LC1_S355HF_250x150x5	N (100%)	0_0	1477	1499	0.98
4	RHS_LC1_S355HF_200x100x5	N (100%)	0_0	1159	1143	1.01
5	SHS_LC1_S355CF_200x200x5	N (100%)	0_0	1300	1307	0.99
6	SHS_LC1_S355CF_200x200x6	N (100%)	0_0	1936	1967	0.98
7	SHS_LC1_S355HF_200x200x5	N (100%)	0_0	1604	1603	1.00
8	SHS_LC1_S355HF_200x200x6.3	N (100%)	0_0	2168	2141	1.01
9	CHS_LC1_S355CF_159x6.3	N (100%)	0_0	1788	1727	1.03
10	CHS_LC1_S355HF_159x6.3	N (100%)	0_0	1531	1519	1.00
11	CHS_LC1_S355HF_159x5	N (100%)	0_0	1284	1228	1.04
12	CHS_LC1_S355HF_159x7.1	N (100%)	0_0	1637	1597	1.02
13	RHS_LC2_S355CF_200x100x4	N (50%) + M_y (50%)	60_0	597	595	1.00
14	RHS_LC2_S355CF_220x120x6	N (50%) + M_y (50%)	67_0	1160	1141	1.01
15	RHS_LC2_S355HF_250x150x5	N (50%) + M_y (50%)	47_0	1063	1052	1.01
16	RHS_LC2_S355HF_200x100x5**	N (50%) + M_y (50%)	65_0	-	-	-
17	SHS_LC2_S355CF_200x200x5	N (50%) + M_y (50%)	77_0	816	848	0.96

18	SHS_LC2_S355CF_200x200x6	N (50%) + M_y (50%)	72_0	1179	1218	0.96
19	SHS_LC2_S355HF_200x200x5	N (50%) + M_y (50%)	62_0	942	932	1.01
20	SHS_LC2_S355HF_200x200x6.3	N (50%) + M_y (50%)	60_0	1302	1272	1.02
21	CHS_LC2_S355CF_159x6.3	N (50%) + M_y (50%)	45_0	1060	1056	1.00
22	CHS_LC2_S355HF_159x6.3	N (50%) + M_y (50%)	50_0	747	787	0.94
23	CHS_LC2_S355HF_159x5	N (50%) + M_y (50%)	41_0	725	705	1.02
24	CHS_LC2_S355HF_159x7.1**	N (50%) + M_y (50%)	50_0	-	-	-
25	RHS_LC3_S355CF_200x100x4	N (33%)+M_y (33%)+M_z (33%)	63_39	420	408	1.02
26	RHS_LC3_S355CF_220x120x6	N (33%)+M_y (33%)+M_z (33%)	72_40	851	861	0.98
27	RHS_LC3_S355HF_250x150x5	N (33%)+M_y (33%)+M_z (33%)	82_50	623	630	0.98
28	RHS_LC3_S355HF_200x100x5	N (33%)+M_y (33%)+M_z (33%)	48_25	589	606	0.97
29	SHS_LC3_S355CF_200x200x5	N (33%)+M_y (33%)+M_z (33%)	62_60	771	792	0.97
30	SHS_LC3_S355CF_200x200x6	N (33%)+M_y (33%)+M_z (33%)	65_65	1069	1082	0.98
31	SHS_LC3_S355HF_200x200x5	N (33%)+M_y (33%)+M_z (33%)	60_60	829	812	1.01
32	SHS_LC3_S355HF_200x200x6.3	N (33%)+M_y (33%)+M_z (33%)	50_50	1069	1078	0.98
33	CHS_LC3_S355CF_159x6.3	N (33%)+M_y (33%)+M_z (33%)	50_45	893	881	1.01
34	CHS_LC3_S355HF_159x6.3	N (33%)+M_y (33%)+M_z (33%)	50_50	623	653	0.95
35	CHS_LC3_S355HF_159x5	N (33%)+M_y (33%)+M_z (33%)	40_40	619	610	1.01
36	CHS_LC3_S355HF_159x7.1	N (33%)+M_y (33%)+M_z (33%)	50_50	705	717	0.98
37	2_SHS_LC1_S355CF_200x200x6	N (100%)	0_0	1954	1974	0.99
38	2_SHS_LC2_S355CF_200x200x6	N (50%) + M_y (50%)	71_0	1194	1143	1.04
39	2_SHS_LC3_S355CF_200x200x6	N (33%)+M_y (33%)+M_z (33%)	62_62	1076	1102	0.97
40	RHS_LC4_S355CF_220x120x6	N (50%) + M_z (50%)	0_40	972	970	1.00
41	RHS_LC5_S355CF_220x120x6	N (50%)+M_y (25%)+M_z (25%)	33_20	1182	1231	0.96
42	RHS_LC6_S355CF_220x120x6	N (80%)+M_y (10%)+M_z (10%)	10_6	1606	1581	1.01
43	RHS_LC4_S355CF_200x100x4	N (50%) + M_z (50%)	0_35	471	470	1.00
44	RHS_LC5_S355CF_200x100x4	N (50%)+M_y (25%)+M_z (25%)	31_19	625	605	1.03
45	RHS_LC6_S355CF_200x100x4	N (80%)+M_y (10%)+M_z (10%)	6_5	763	769	0.99
46	RHS_Stub_S355CF_200x100x4	Stub column- N (100%)	0_0	761	788	0.96
47	RHS_Stub_S355CF_220x120x6	Stub column- N (100%)	0_0	1648	1546	1.06
48	RHS_Stub_S355HF_250x150x5	Stub column- N (100%)	0_0	1358	1380	0.98
49	RHS_Stub_S355HF_200x100x5	Stub column- N (100%)	0_0	1163	1164	0.99
50	SHS_Stub_S355CF_200x200x5	Stub column- N (100%)	0_0	1296	1350	0.96
51	SHS_Stub_S355CF_200x200x6	Stub column- N (100%)	0_0	1957	2002	0.97
52	SHS_Stub_S355HF_200x200x5	Stub column- N (100%)	0_0	1607	1615	0.99
53	SHS_Stub_S355HF_200x200x6.3	Stub column- N (100%)	0_0	2227	2194	1.01
54	CHS_Stub_S355CF_159x6.3	Stub column- N (100%)	0_0	1800	1872	0.96
55	CHS_Stub_S355HF_159x6.3	Stub column- N (100%)	0_0	1560	1543	1.01
56	CHS_Stub_S355HF_159x5	Stub column- N (100%)	0_0	1255	1187	1.05
57	CHS_Stub_S355HF_159x7.1	Stub column- N (100%)	0_0	1632	1538	1.06

*e_y represents the adopted eccentricity along y-y axis, e_z is the adopted eccentricity along z-z axis

** No available results recorded due to unexpected technical and electrical difficulties with the recording software

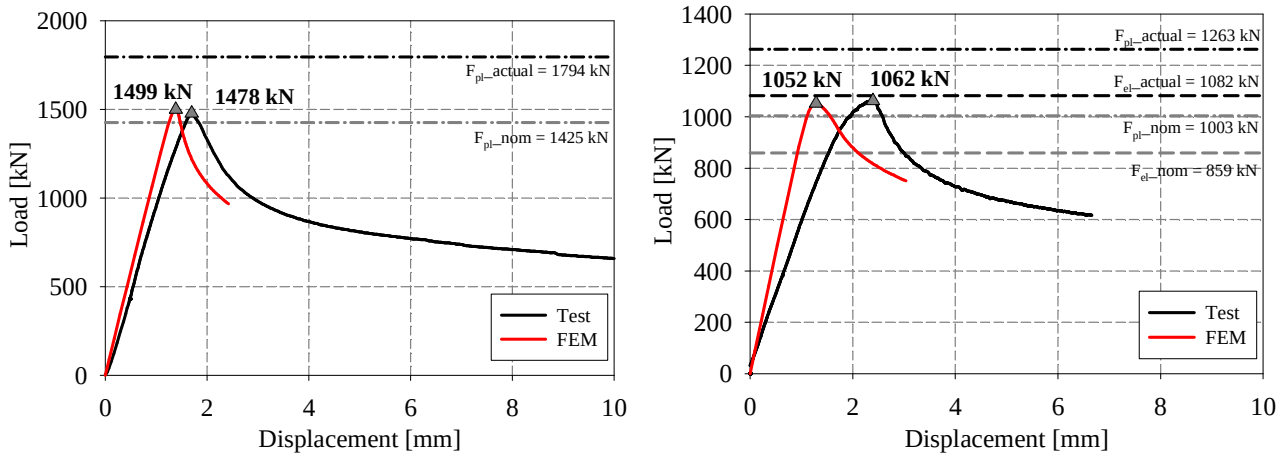

Figure 8: Numerical vs. experimental load displacement curves a) specimen LC1_RHS_250x150x5_HF – b) LC2_RHS_250x150x5_HF

3. Development and validation of shell FE models

3.1 Shell modelling

To select the proper FE mesh that provides accurate results with minimum computational time, five different mesh configurations were considered and the adequate type of meshing was selected.

In order to represent accurately the experimental behaviour of the specimens, a suitable FE-model had to be developed. The endplates were represented through rigid plates having an equivalent thickness of 80 mm and modelled with shell elements that remain elastic during loading. The plates' stiffness allowed an even distribution of the applied load at the ends of the sections and prevented the cross-sectional deformation at both ends while allowing free rotations. As for the behaviour of the hinges, truss elements were used to simulate the rigid spherical hinges at both ends. All trusses were connected to the rigid end plates nodes and to the centroid of the hinge (see Figure 9). The load was applied at the centroid of the hinge, and the combined loads cases with compression were represented through an axial load applied at the centroid of the hinge with the corresponding measured test eccentricities.

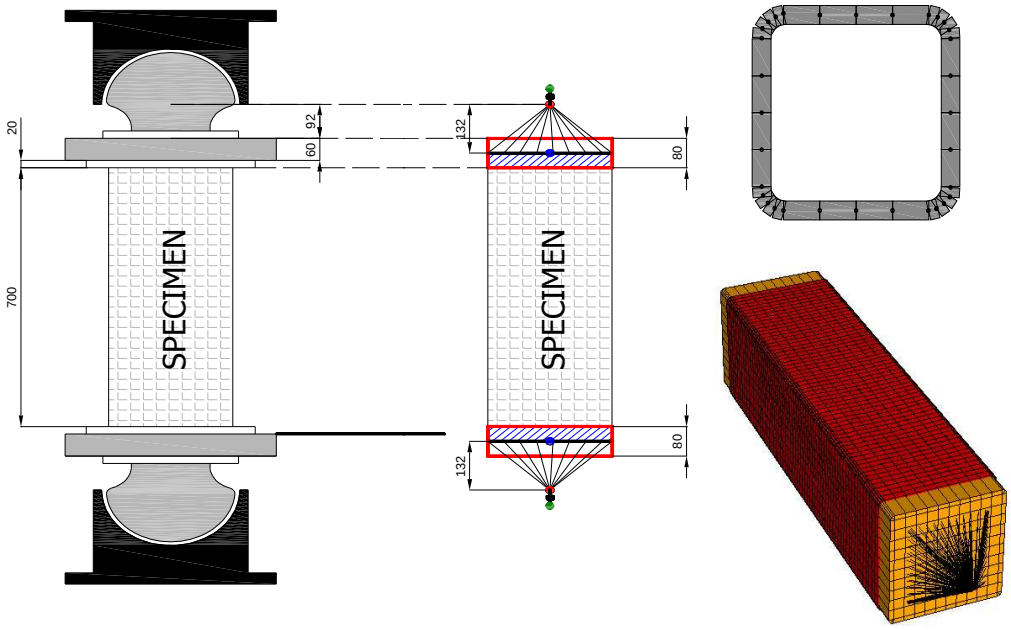

Figure 9: Finite element model assumptions

Series of numerical computations have been performed with the use of non-linear FEM software FINELg, continuously developed at the University of Liège and Greisch Engineering Office since 1970 (Greish and Ulg, Finelg 1999). This software offers almost all types of FEM types of analyses, and present investigations have mainly been resorting to so-called MNA (Materially Non-linear Analysis), LBA (Local Buckling Analysis) and GMNIA (Geometrically and Materially Nonlinear Analysis with Imperfections) analyses. The cross-sections were modelled with the use of quadrangular 4-nodes plate-shell finite elements with typical features (corotational total Lagrangian formulation, Kirchhoff's theory for bending). The corners of square and rectangular profiles were modeled with 4 linear shell elements per corner (see Figure 9).

Averaged measured geometrical dimensions were used in the calculations, together with measured local imperfections and residual stresses for each specimen (see Figure 10).

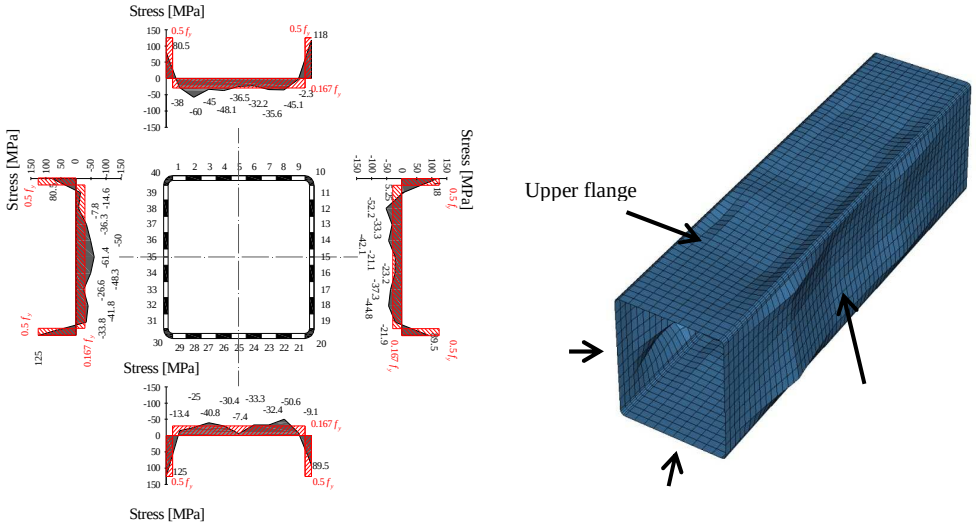

Figure 10: a) adopted membrane stresses in the finite element computation of the specimen SHS_HF_200x200x6.3 – b) 3D amplified imperfect shape of the specimen SHS_HF_200x200x6.3 (scale factor: 15)

Averaged measured material stress-strain behavior including strain-hardening effects was also included. For the cold-formed tubular profiles, two material laws have been defined; one for the base material and one for the corner regions. A Simple Ramberg-Osgood material law was used for the flat regions and a multi-linear law was adopted for the corner regions.

3.2 Validation: test vs. FE predictions

The experimental cross-section capacities reached by the tested specimens were compared to the numerically-predicted ones. The ultimate loads and the ratio of the experimental ultimate loads to their numerical counterparts are given for the tested cross-sections in Table 2. As previously mentioned, all numerical simulations of the specimens were based on actual cross-sectional dimensions and actual material properties. Numerical simulations represented the real behavior quite accurately. A graphical comparison of the ultimate loads of the FE-simulations and of the experiments is shown in Figure 11 in which the red lines indicate a deviation of +/- 10%.

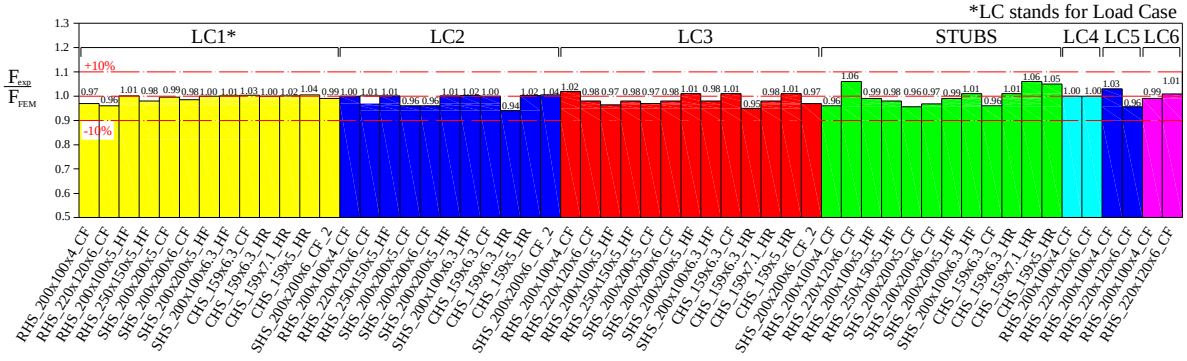

Figure 11: FE peak loads vs. experimental loads

It can be seen that all numerical simulations provide ultimate loads in excellent accordance with the test results. All values oscillate very closely to the $F_{exp} / F_{FEM} = 1.0$ line, which indicates a very good accordance between test and numerical results.
Figure 8 provides representative examples of experimental and numerical load-displacement curves. The differences in initial stiffness, ultimate load and post-peak behavior between numerical and experimental results are mainly caused by non-explicitly modeled sources, such as a little friction in the hinges (i.e. the boundary conditions are never as clean as in the computational model and are far more complicated than assumed in the numerical model), inconsistencies in the imperfections measurements, unexpected eccentricities, non-homogenous material... In particular, the numerical model is assumed to be free from any friction in the hinges – preliminary measurements showed that friction could be neglected; the complete test set-up stiffness was also not modeled. Since a maximum deviation of 6% among all F_{exp} / F_{FEM} values is reported, the ability of the numerical models to accurately predict the failure load is obvious.

4. Assessement of proposed design approach

4.1 FE parametric studies

The finite element model was further used to generate an extensive set of numerical cross-section tests to investigate deeply the structural behaviour of cross-sections belonging to all classes defined according to the Eurocode 3 classification system (EN 1993-1-1 2005). The numerical study concerns hot-rolled and cold-formed sections having nominal geometrical dimensions and various parameters with the target of analyzing their physical behavior. The parameters were chosen in order to cover all four classes' ranges with different load cases going from simple to combined ones. These numerical computations provided a basis for the generation of several design models.

A derived FE-model has been implemented on the basis of the validated one. Quadrangular four node shell elements with corotational total Lagrangian formulation have been adopted in all simulations. Regarding longitudinal displacements in the end section nodes, a numerical modeling resorting to kinematic linear constraints has been developed. The end cross-section only exhibits a maximum of three degrees of freedom: axial global displacement, rotation about the strong axis and rotation about the weak axis. Only three different nodes are then necessary to describe the displacement of any point in the cross-section once the linear relationships for axial displacements are established. In other words, a maximum of three nodes may experience a "free" longitudinal displacement, while all other nodes' x-displacements linearly depend on the longitudinal displacements of the "x-free" nodes to respect a global cross-sectional displaced configuration. The three "x-free" nodes were chosen at the plate edges (at the beginning of different corners) of the cross-section, and all the nodes in between were constrained to the three main nodes with respected linear relationships (see Figure 12).
Additional fictitious nodes have been defined at the centroids of the end-cross-sections for the definition of the (ideal) support conditions, and transverse supports preventing from local buckling have also been implemented. This modeling technique was validated and adopted successfully in various previous FE studies (Semi-comp 2007).

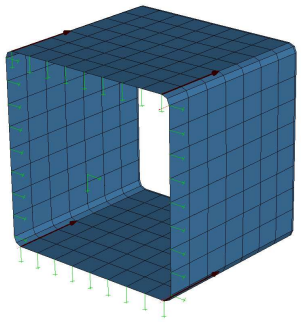

Figure 12: Support conditions and external load application

The same mesh density as described above was used in all simulations. Initial geometrical imperfections have been basically introduced through adequate modifications of node coordinates. Since local buckling failure modes shall be reached in any situation from plastic to slender section geometries, only local geometrical imperfections have been adopted and were defined as square half-wave patterns in both directions of the flanges and webs, with an amplitude of a / 200, where a stands for the length of the considered "square" panel (see Figure 13)

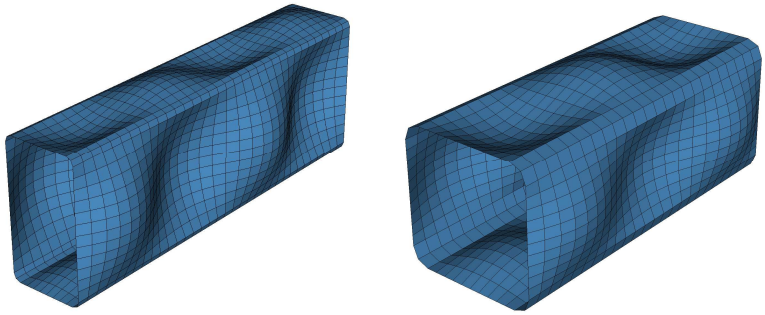

Figure 13: Local geometrical imperfections adopted for both square and rectangular hollow sections

Then, parametric numerical calculations have been carried out for the cross section resistance of various section shapes, dimensions and steel grades. Firstly, 296 tubular geometries picked up from the European catalogue were considered with 156 rectangular cross sections alongside 140 square cross sections.

Secondly, an additional set of derived (invented) sections was considered. This was intended at a better visualization of more distributed results along higher slenderness, because the European sections would be covering only a limited range of cross-section slenderness. Thus, the proposed sections have been derived with respect to the *h/b* and *b/t* ratios; 5 values of h/b ranging from square sections to highly rectangular ones, have been considered: *h/b=1*, *1.5*, *2*, *2.5* and *3*. For each *h/b* proposed value, *b/t* values spanning from 15 to 115 with a step of 2 have been considered for the load cases of pure compression and major axis bending, and values going from 15 to 115 with a step of 4 for the load cases of minor axis bending and combined compression and bi-axial bending.

The following set of parameters has been considered for these sections:

- 3 different steel grades: S235, S355, S460;

- Different loading conditions: pure compression, major axis bending, minor axis bending, compression and major axis bending, compression and minor axis bending, compression and bi-axial bending.

For the combined load cases, a difference was made between the different loading situations, namely with respect to the degree of bi-axiality, i.e. the M_y / M_z ratio; this ratio was varied on the basis of α angles of 0, 30, 50, 70 and 90 degrees between plastic capacities $M_{pl,y}$ and $M_{pl,z}$ as shown in Figure 14. As for the non-dimensional influence of axial force n, 6 values were adopted going from 0 (i.e. $N / N_{pl}=0$, the load case thus becoming a biaxial bending $M_y + M_z$ case) to 90 (i.e. $N / N_{pl}=90\%$, the load case becoming thus a compression of 90% N_{pl} with biaxial bending M_y+M_z one). The adopted intermediate values are shown in Table 3. The following denomination will be adopted for the distinction of the various combined load cases:

$$nx\_\alpha \tag{1}$$

where x represents the non-dimensional axial force in percentage, and α is the angle representing the degree of bi-axiality (in degrees), as shown in Figure 14. For example n50_30, refers to a combined load case of 50% N_{pl} with a degree of bi-axiality characterized by an angle of 30 degrees. It has to be noted that the loading was applied proportionally for all combined load cases. Table 3 represents the adopted cases for the European and derived sections. In total, some 40 000 non-linear shell calculations have been performed.

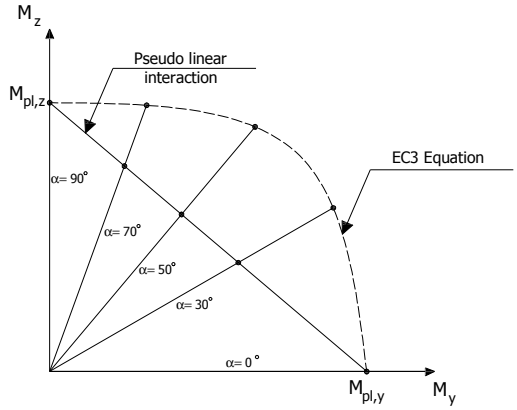

Figure 14: Selection of load cases for N + M_y + M_z combined situations

Table 3: Adopted combined load cases for European and derived section.

		α				
		0	30	50	70	90
n	0	D	D	D	D	D
	20	D-E	D-E	D-E	D-E	D-E
	40	D	D	D	D	D
	60	D-E	D-E	D-E	D-E	D-E
	80	D	D	D	D	D
	90	D	D	D	D	D

*D stands for derived sections, and E stands for European sections

Figure 15 and Figure 16 show all gathered numerical results relative to hot-rolled and cold-formed cross-sections respectively represented in an O.I.C. format, i.e. the horizontal axis relates to the generalized slenderness $\lambda_{rel,CS}$, while the vertical axis reports on the cross-section reduction factor χ_{CS} (see Figure 1).

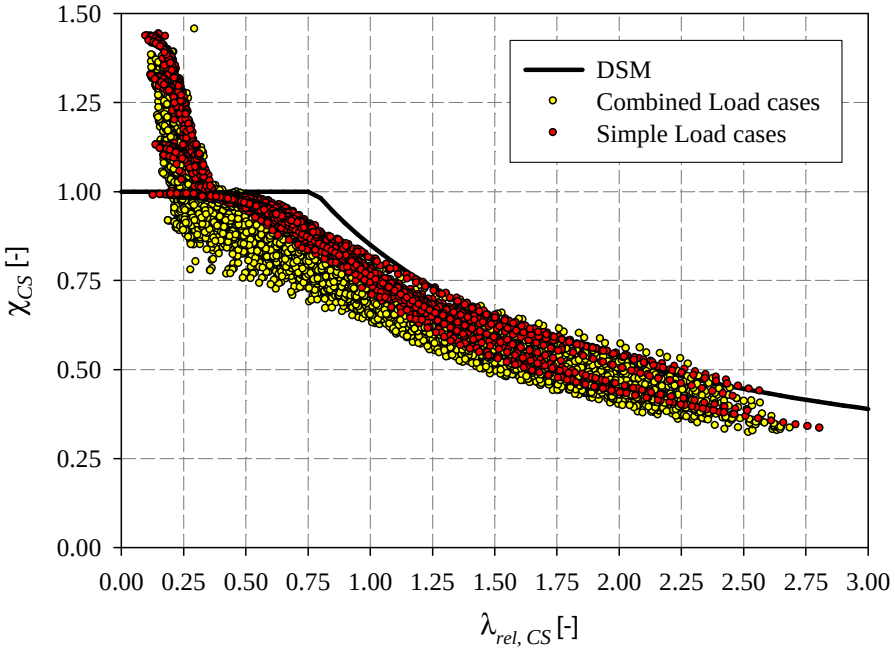

Figure 15: Numerical results relative to hot-rolled cross-sections

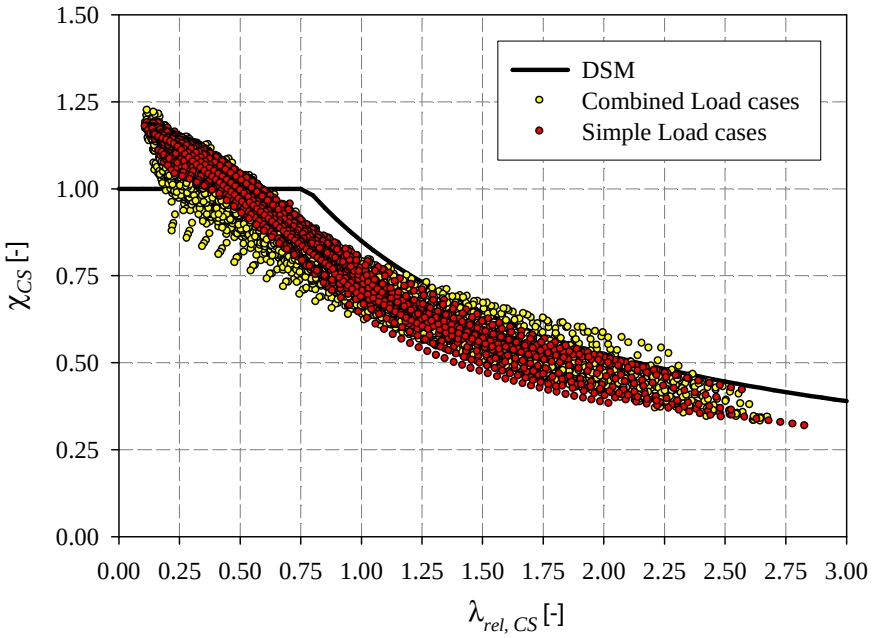

Figure 16: Numerical results relative to cold-formed cross-sections

4.2 Analysis of results and governing parameters

The results relative to hot-rolled sections are only presented in this section for sake of clarity and because of available space limitations. The present analyses address the influence of the yield stress, the cross-section shape, and the load case type. The difference in the structural response between fabrication processes is mainly accounted for through the material and the residual stress distributions in the numerical simulations.

Figure 17 proposes the obtained numerical results for square sections in compression with the target of analyzing the influence of the yield stress. One may notice a relatively really small scatter in the results. Smooth and clear tendencies may be observed in other situations as well, e.g. RHS or different load cases. The influence of the yield stress is only pronounced as a general trend, for small relative slenderness values with $\lambda_{CS} < 0.4$. In other words, an important level of over-strength due to strain hardening effects is observed for low steel grades.

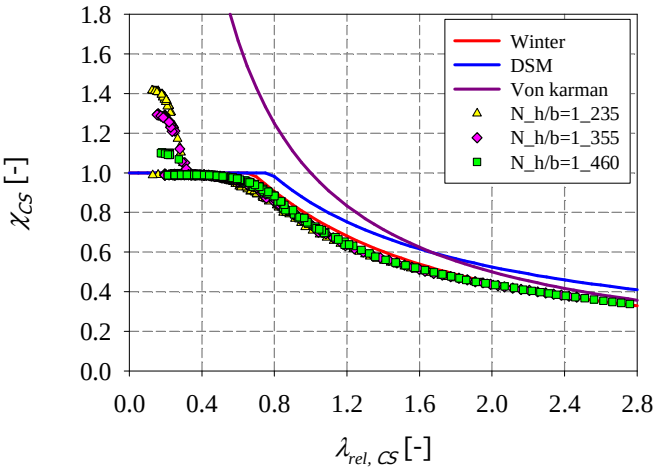

Figure 17: FE results for square sections under pure compression, represented in function of different yield stresses

Concerning the influence of the cross-section shape, it is shown that rectangular hollow sections ($h / b > 1$) subjected to pure compression (see Figure 18a) reach higher relative section resistance compared to square hollow sections possessing the same relative slenderness, particularly in the slender range. The level of restraint offered by the narrow faces of the rectangular section to the wider ones is therefore shown to provide an increased cross-section resistance through stress redistributions once local buckling develops in the more buckling-prone plates. Consequently, the cross-section resistance is increased with the h/b ratio, and square sections exhibit the lowest resistance to compression ($h/b=1.0$) owing to simultaneous buckling of the constitutive plates.

For major-axis bending cases, the opposite is shown in Figure 18b: the square hollow sections are seen to achieve higher relative bending resistances than the rectangular ones possessing the same cross-section slenderness, particularly in the slender range. The load case definition plays a delicate role here, and shows to be decisive for the structural behavior of elements. In contrary to the compression case, the compressed flanges in the strong axis bending load cases find themselves in need to a great restraint from the webs which in turn possess higher slenderness in rectangular sections compared to square ones.

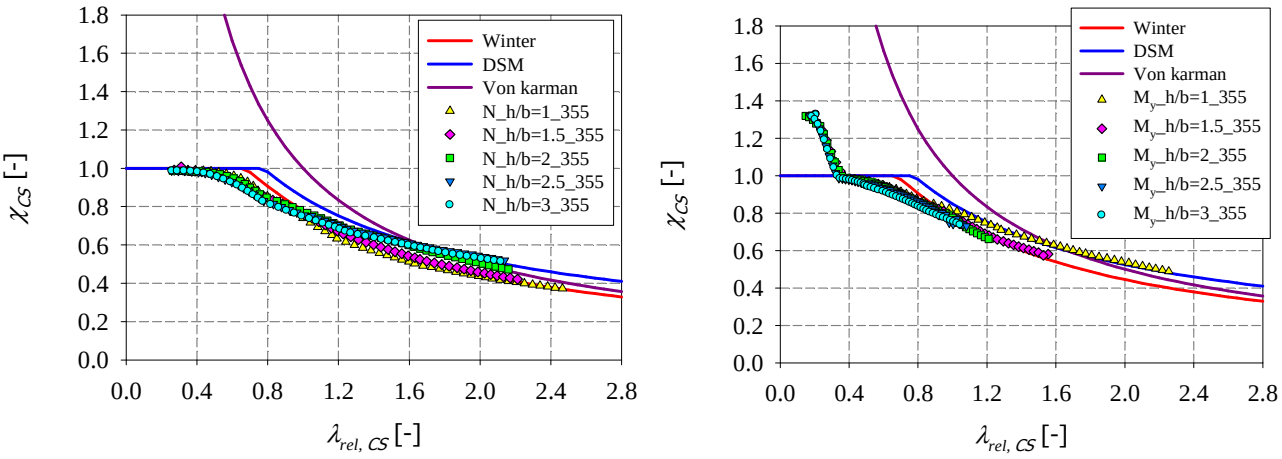

Figure 18: a) FE results for square and rectangular sections under compression, varying aspect ratios, S355, – b) FE results for square and rectangular sections under major axis bending moment, varying aspect ratios, S355

Consequently, the restraint provided by the webs to the flanges will be greater in the case of square sections, delaying the onset of local buckling. This is pronounced for slender sections, where failure occurs largely within the elastic material range. For stocky sections, failure will be attained at higher strains, where plasticity leads the structural behavior, reducing the detrimental restraint brought to the flanges.

Finally, concerning the load case impact, the influence of the relative axial compression is obvious but the results on Figure 19a still show a small dispersion and clear tendencies may be emphasized.

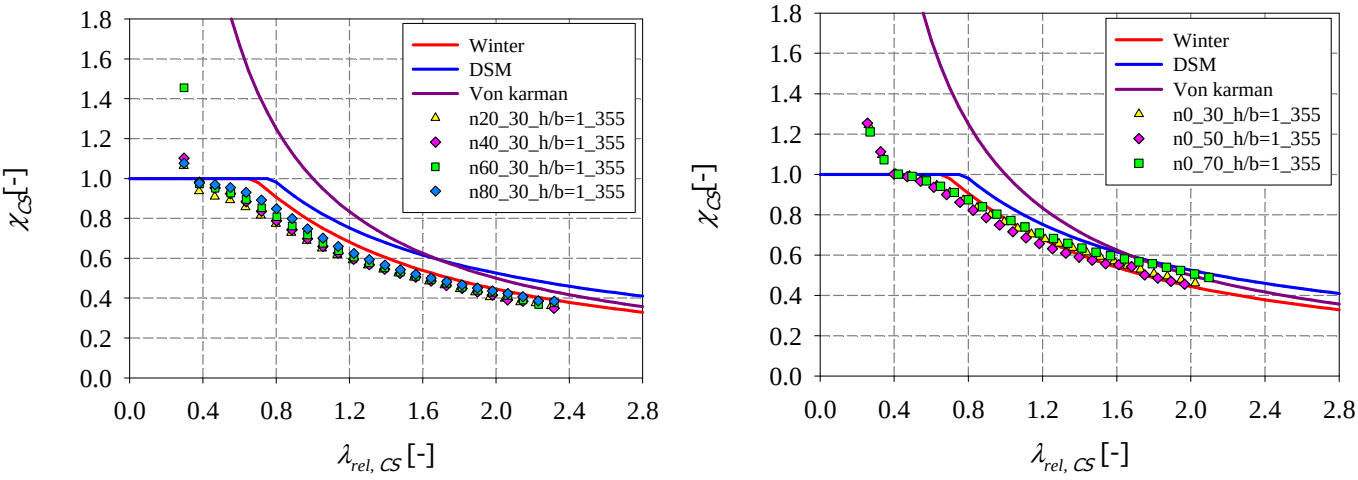

Figure 19: a) FE results for square sections under combined load cases with a varying level of axial forces, S355, – b) FE results for square sections under combined load cases with a varying level of bi-axialty, S355

Figure 19b presents results for which no axial compression is present, i.e. biaxial bending situations; it allows evidencing the influence of the degree of biaxiality in square sections. Ideally, very close tendencies should be observed, and a quite limited scatter is expected for

$\alpha = 30$ and $\alpha = 70$. As can be seen in Fig. 18, differences appear, especially for large λ_{CS} values. This is to be attributed to the initial geometrical imperfections (i.e. inward buckles in the flanges and outward buckles in the webs or vice-versa), which can be shown to lead to slightly different structural responses, depending on the outward-inward buckling pattern.

5. Design proposal background

The well-known Ayrton-Perry formula format has been selected as a basis for the derivation of the O.I.C.-based formulae. It contains a simple yet accurate way of considering both failure limits to be defined, with the corresponding end-of-plateau value and imperfection factor. Even the resistance limit and the instability limit can be adapted to the observed trends in the reference results. Therefore, the following four variables were incorporated into the Ayrton-Perry formula (see Figure 20):

1- The end-of-plateau λ_0 value;
2- The imperfection factor α;
3- The instability limit, since some cross-sections may exhibit post-buckling reserves higher than the post-buckling reserve determined in the Von Karman formula relative to plates. Thus, a factor needs to be added in the Von Karman formula, to account for a possible variation of the instability limit;
4- The resistance limit, since stocky cross-sections usually gain from strain hardening effects so that $\chi_{CS} > 1.0$ predictions may be appropriate.

The corresponding 'extended' Ayrton-Perry formula then becomes the following:

$$(\beta - \chi)\left(1 - \chi\lambda^{\delta}\right) = \eta\chi \tag{2}$$

Where β is the constant or equation defining the resisting limit, δ the exponent added to the Von Karman format for the consideration of different instability limits, and η the factor accounting for imperfections.

Eq. 2 can be rearranged in the following form:

$$\chi = \frac{\beta}{\phi + \sqrt{\phi^2 - \lambda^{\delta}\beta}} \tag{3}$$

With $\phi = 0.5\left(1 + \alpha\left(\lambda - \lambda_0\right) + \lambda^{\delta}\beta\right)$

The derivation of adequate design curves based on this simple yet mechanical background (i.e. local calibration of λ_0, δ and α factors) is currently in progress.

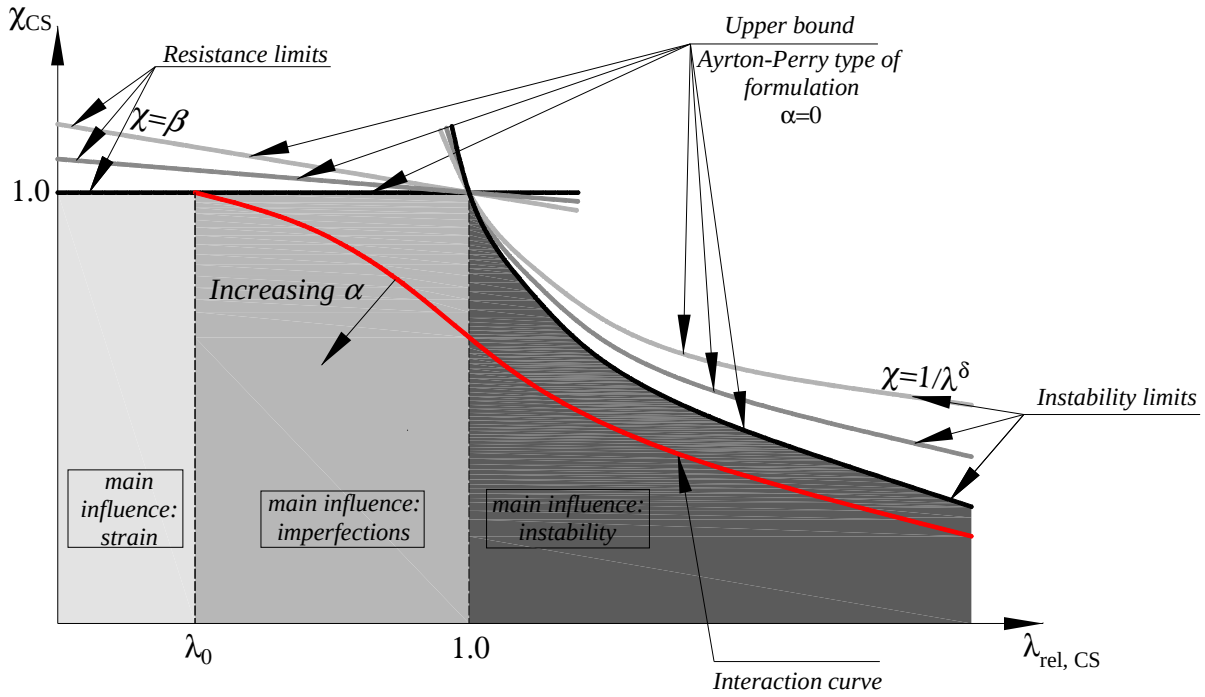

Figure 20: Schematic representation of the adopted Ayrton-Perry approach

6. Conclusions

In the present paper, an experimental test program on rectangular, square and circular hollow sections of grade S355 structural steel was reported. Hot-finished, hot-rolled and cold-formed stub columns as well as cross-section tests with various load cases (compression, compression + major axis-bending, compression + minor-axis bending, compression + biaxial bending) were described. Moreover, the measurements of material constitutive laws (tensile tests), imperfections and residual stress measurements were reported.

Besides, a numerical model was developed to simulate the experimental tests and excellent agreement between both sources demonstrated the appropriateness of the FE models to accurately represent the real behavior of hollow structural shapes under simple and combined loading.

Consecutive extensive FE parametric studies on hot-rolled and cold-formed hollow sections were presented and contributed to evidence the potential for the Overall Interaction Concept to become a reliable and practical alternative to the current well-known design rules, in particular with respect to resistance-instability interactions. The design proposal background was then presented and is based on the Ayrton-Perry approach applicable in standards for members, and adapted to represent accurately the cross-section capacity of tubular members.

References

AISC (2005). Specification for structural steel buildings. *American Institute of Steel Construction*, Chicago, IL. ANSI/ASIC 360-05.

Bebiano, Pina, Silvestre & Camotim (2008). "GBTUL – Buckling and Vibration Analysis of Thin-Walled Members", DECivil/IST, Technical University of Lisbon (http://www.civil.ist.utl.pt/gbt).

Boissonnade 2011. “The Concept of Cross-section Classes in Eurocode 3 into Question”, *ECCS TC8 meeting*, Lisbon, June 3rd.

Boissonnade, Nseir & Saloumi (2013). “The Overall Interaction Concept: an Alternative Approach to the Stability and Resistance of Steel Sections and Members”. *Proceedings of the Annual Stability Conference*, Structural Stability Research Council, St. Louis, Missouri, April 16-20.

CEN (Comité Européen de Normalisation. (2005). “Eurocode 3: Design of Steel Structures, Part 1–1: General rules and rules for buildings (EN 1993-1-1)”, Brussels.

Cidect report (2014a), Project “HOLLOPOC” – Hollow profiles Overall Concept – 1st interim report, Part A: cross-sectional resistance – Experiemental tests and validation of FE models.

Cidect report (2014b), Project “HOLLOPOC” – Hollow profiles Overall Concept – 1st interim report, Part B: cross-sectional resistance – FE parametric studies on hot-formed RHS and SHS shapes.

Gardner (2008). “The continuous strength method”. *Proc. Institution of Civil Engineers: Structures and Buildings*, vol. 161, n°3, p 127-133.

Kettler 2008. “Elastic-plastic cross-sectional resistance of semi-compact H- and hollow sections”. *PhD Thesis*, Graz Technical University.

Li & Schafer (2010) “Buckling analysis of cold-formed steel members with general boundary conditions using CUFSM: conventional and constrained finite strip methods.” *Proceedings of the 20th Int. Spec. Conf. on Cold-Formed Steel Structures*, St. Louis, MO. November.

Rasmussen & Hancock (1993) “Design of cold-formed Stainless Steel Tubular Members I:columns”, *Journal of Structural Engineering, Americal Society of Civil Engineers*, Vol. 119, pp 2349-2367.

Rasmussen & Hancock (1993) “Design of cold-formed Stainless Steel Tubular Members II: Beams”, *Journal of Structural Engineering, Americal Society of Civil Engineers*, Vol. 119, pp 2368-2386.

Schafer (2006) “Cross-section Stability of Structural Steel”, AISC Faculty Fellowship Research Project.

Semi-Comp (2007) “Plastic member capacity of semi-compact steel sections – a more economic design (Semi-Comp)”. 2007. *Final report (01/01/06 – 30/06/07)* – RFCS – Steel RTD (Contract RFS-CR-04044).

S.T.S.S. (2012). “Research project STSS – Simple Tools Sell Steel” (http://www.ims.org/2012/02/stss-simple-tools-sell-steel/).